PCCP

ROYAL SOCIETY OF CHEMISTRY

PAPER

View Article Online
View Journal

Cite this: DOI: 10.1039/d6cp01016d

Osmotic coefficient and mean ionic activity coefficient of supersaturated ammonium nitrate solutions measured by laser trapping and Raman spectroscopy

Kento Kuniyoshi and Shoji Ishizaka *

We report thermodynamic measurements for supersaturated aqueous ammonium nitrate (NH_4NO_3) solutions in single micrometer-sized droplets levitated in air by laser trapping at 298 K. Water activity (a_w) was obtained directly from the gas-phase relative humidity as the humidity was systematically reduced. Droplet composition was quantified by *in situ* Raman spectroscopy: spectral deconvolution was used to determine the NO_3^-/H_2O peak-area ratio, which was converted to nitrate concentration using a calibration curve constructed from bulk solutions of known concentration. This approach enables access to ultra-high molalities up to m = 215 mol kg^{-1}, corresponding to a total ionic mole fraction x_I = 0.89. The a_w data agree with literature values over x_I = 0.20–0.67, whereas systematic differences relative to electrodynamic-balance datasets appear at higher x_I, where volatilization of NH_4NO_3 (*via* NH_3 and HNO_3 loss) and other non-ideal processes may become increasingly important. Using the measured composition – a_w relationship, we derive the osmotic coefficient (ϕ) and the mean molal ionic activity coefficient ($\gamma_\pm$) across the full concentration range, providing new benchmarks for modeling highly concentrated NH_4NO_3 relevant to aerosol thermodynamics.

Received 20th March 2026,
Accepted 16th April 2026

DOI: 10.1039/d6cp01016d

rsc.li/pccp

1. Introduction

Cloud droplets and aerosol water droplets can dissolve a wide range of solutes, which depress the equilibrium vapor pressure of water and hence reduce the water activity (a_w). In airborne microdroplets, the absence of contact with solid substrates can suppress heterogeneous crystallization, allowing droplets to persist as metastable liquids at solute concentrations exceeding bulk solubility. Under such highly concentrated conditions, ion–ion interactions become non-negligible, and solution non-ideality must be described in terms of activities rather than concentrations.

Ammonium nitrate (NH_4NO_3) is one of the major inorganic constituents of atmospheric particulate matter, and its semi-volatile nature makes the gas–particle partitioning of nitrate a key process influencing air pollution and climate.[1,2] Recent studies have shown that this partitioning is sensitive to the activity coefficients of NH_4NO_3, while appreciable discrepancies remain among thermodynamic model predictions under highly concentrated conditions.[3] Consequently, experimental constraints on the activity coefficients of aqueous NH_4NO_3, particularly in the supersaturated regime, are highly desirable. Quantitative knowledge of the thermodynamic properties of supersaturated NH_4NO_3 solutions—including a_w, osmotic coefficient (ϕ), and mean molal ionic activity coefficient ($\gamma_\pm$)—is therefore essential for understanding aerosol–cloud interactions at low relative humidity.

At 25 °C, the solubility limit of ammonium nitrate corresponds to a molality of 26 mol kg^{-1}.[4] Up to this concentration, osmotic coefficients and mean ionic activity coefficients of aqueous NH_4NO_3 have been determined primarily by isopiestic measurements, and experimental values are available in the literature.[4,5] In the supersaturated concentration regime, however, direct measurements of osmotic coefficients and mean ionic activity coefficients are much more limited. Chan *et al.* extended measurements to ~111 mol kg^{-1} by levitating single micrometer-sized NH_4NO_3 solution droplets in air using an electrodynamic balance (EDB), thereby eliminating contact with solid surfaces and suppressing crystallization.[6] Such contact-free levitation techniques provide a powerful means of probing thermodynamic properties of metastable supersaturated aqueous solutions that are difficult to access in bulk experiments. To the best of our knowledge, the EDB data reported by Chan *et al.* (up to ~111 mol kg^{-1} at 25 °C) represent the highest-concentration direct measurements available at 25 °C for

Graduate School of Advanced Science and Engineering, Hiroshima University, 1-3-1 Kagamiyama, Higashi-Hiroshima 739-8526, Japan.
E-mail: ishizaka@hiroshima-u.ac.jp

osmotic coefficient and mean ionic activity coefficient of aqueous NH_4NO_3.

Aqueous droplets containing NH_4NO_3 in air approach equilibrium with the surrounding gas phase when the water vapor pressure at the droplet surface matches that of the ambient air. Therefore, as the relative humidity (RH) is gradually decreased, water evaporates from the droplet and the NH_4NO_3 concentration increases. Upon continued dehydration, the solution can enter a supersaturated regime and may eventually undergo a liquid-to-solid phase transition, commonly referred to as efflorescence.[7] Previous studies have reported efflorescence of NH_4NO_3 particles over a range of RH values,[6,8,9] whereas other studies have shown that NH_4NO_3 particles may not effloresce but instead persist in an anhydrous liquid state.[10–14] Lightstone *et al.* demonstrated using an electrodynamic balance that, when single NH_4NO_3-containing droplets are levitated in air and heterogeneous nucleation due to impurities is rigorously minimized, the droplets can avoid efflorescence and instead form an anhydrous liquid droplet state.[14] They also reported a measurable decrease in particle mass during dehydration–rehydration cycles, indicating volatilization of NH_4NO_3 *via* loss of NH_3 and HNO_3 to the gas phase, which must be accounted for when interpreting thermodynamic measurements. Despite these important findings, a quantitative determination of the concentration dependence of the osmotic coefficient and the mean ionic activity coefficient for supersaturated aqueous NH_4NO_3 was not established.

We have demonstrated that laser trapping coupled with Raman spectroscopy enables *in situ* tracking of hygroscopic phase transitions of single airborne salt particles under controlled RH, including efflorescence and deliquescence of NaCl/$NaNO_3$ mixture particles.[15] Using the same experimental setup in the present work, we extend this contact-free single-droplet approach to ammonium nitrate (NH_4NO_3), for which interpretation is more challenging because the droplet composition can change *via* volatilization of NH_4NO_3 through loss of NH_3 and HNO_3 during dehydration.[12,14,16,17] *In situ* Raman spectroscopy provides a powerful means of constraining the evolving composition of individual droplets when deriving thermodynamic properties.[18–22] Building on this rationale, we hypothesized that optically levitated NH_4NO_3 droplets would allow direct determination of the osmotic coefficient (ϕ) and mean molal ionic activity coefficient ($\gamma_\pm$) at molalities exceeding 111 mol kg^{-1}, *i.e.*, beyond the highest-concentration direct measurements previously available at 25 °C. In addition to the osmotic coefficient and the mean molal ionic activity coefficient, the directly measured water activity data at known droplet compositions provide valuable constraints for the development, parameterization, and validation of semi-empirical thermodynamic models.

In this study, we employ laser trapping and Raman spectroscopy to quantify *in situ* the NH_4NO_3 loss from individual levitated droplets during dehydration and, with this compositional constraint, to determine the molality dependence of ϕ and $\gamma_\pm$ for aqueous NH_4NO_3 at 25 °C over an extended supersaturated concentration range. Furthermore, to describe ϕ and $\gamma_\pm$ across the full experimental range, we adopted a binding mean spherical approximation (BIMSA)–based framework, a statistical-mechanical approach that accounts for ion pairing (association) in concentrated electrolyte solutions.[23]

2. Experimental

Water was purified by reverse osmosis and deionization prior to use (Merck Millipore, Milli-Q Integral 3). Ammonium nitrate (NH_4NO_3, 99.5%, FUJIFILM Wako Pure Chemical Corp.) was used without further purification. Laser trapping and Raman spectroscopy measurements of individual aqueous NH_4NO_3 droplets in air were performed using the instrumentation shown in Fig. 1, following the experimental protocol described in a previous publication.[15] An aqueous solution of NH_4NO_3 was aerosolized with an ultrasonic nebulizer (Omron NE-U07) and introduced into a chamber mounted on the stage of an inverted optical microscope (Olympus IX71). Individual

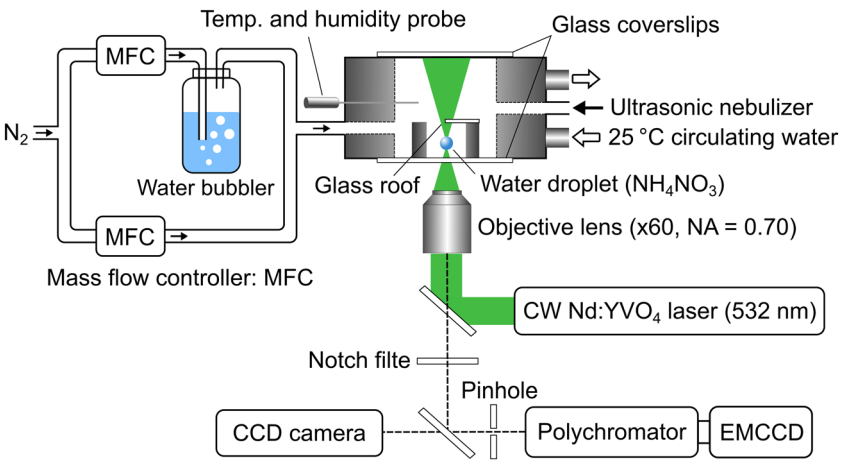

Fig. 1 Schematic illustration of the experimental setup for laser trapping and Raman spectroscopy of single aqueous droplets in air. A micrometer sized droplet is optically levitated by a focused 532 nm CW Nd:YVO_4 laser, while Raman spectra are collected simultaneously to determine droplet composition under controlled relative humidity.

droplets were optically trapped by a focused beam from a CW Nd:YVO_4 laser (532 nm, Coherent Verdi V2) delivered through an objective lens (Olympus LUCPLFLN 60×, N.A. = 0.70). Raman spectra were acquired using a polychromator (SOLAR TII MS3504i, 300 grooves per mm) coupled to an EMCCD detector (Andor DU970N-BV).

The relative humidity (RH) inside the chamber was controlled using a method similar to that reported previously.[19] Nitrogen gas was dried by passing through an air-drying tube packed with cobalt-free silica gel (GL Sciences Inc.) and then split into two streams. One stream was humidified *via* a water bubbler, and the flow rates of both streams were precisely adjusted using mass flow controllers (HORIBA STEC SEC-E40). The streams were recombined and introduced into the chamber at a constant flow rate of 0.500 L min^{-1}. RH and temperature inside the chamber were monitored with a humidity/temperature meter (VAISALA HM42). Bright-field images of NH_4NO_3 droplets during the dehydration process were observed with a CCD camera (TOSHIBA TELI CS9301-03) and recorded as video files on a PC *via* a USB-connected capture device. Changes in droplet size during the dehydration process were analyzed using ImageJ software (NIH, Bethesda, MD, USA). During all experiments, the temperature inside the chamber was maintained at 25.0 ± 0.5 °C by circulating thermostated water (Yamato ThermoElite BH51) through the outer jacket of the chamber.

3. Results and discussion

3.1 Laser trapping and Raman spectroscopy of supersaturated aqueous ammonium nitrate droplets in air

A single droplet was optically trapped in air within the chamber after being introduced *via* an aerosol stream. The stream was generated by an ultrasonic nebulizer that employed an aqueous NH_4NO_3 solution (1.0 mol dm^{-3}) as the stock solution. The droplet gradually increased in size as additional aerosol droplets collided and coalesced with it. Once its diameter reached approximately 20 μm, the nebulizer was turned off to terminate the droplet supply. Next, nitrogen gas with controlled humidity (humidified nitrogen at 0.450 L min^{-1} and dry nitrogen at 0.050 L min^{-1}) was introduced into the chamber, and the system was allowed to equilibrate until the optically trapped droplet attained thermodynamic equilibrium, which required about 60 minutes. Fig. 2(a) presents a microscopic image of the droplet once its size had stabilized at thermodynamic equilibrium. At this stage, the relative humidity within the chamber was 85.0%, and the droplet had a diameter of 18.3 μm.

As noted in our previous study, the solute concentration of an aerosol droplet does not necessarily correspond to that of the stock solution used for its generation.[18] To determine the NH_4NO_3 concentration in the trapped droplet shown in Fig. 2(a), its Raman spectrum was recorded, as shown by the black solid line in Fig. 3. The peaks observed at 717, 1047, and 1393 cm^{-1} are attributed to the bending (ν_4), symmetric stretching (ν_1) and antisymmetric stretching (ν_3) modes of the

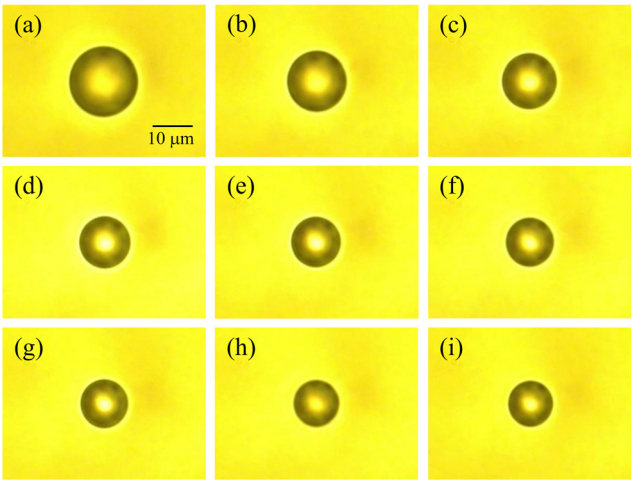

Fig. 2 Snapshots of an NH_4NO_3-containing aqueous droplet levitated in air during the dehydration process at relative humidities of (a) 85.0%, (b) 72.2%, (c) 64.7%, (d) 52.3%, (e) 42.6%, (f) 36.0%, (g) 27.0%, (h) 16.8%, and (i) 7.9%.

NO_3^- ion, respectively.[24] The peak observed at around 1658 cm^{-1} is assigned to the bending mode of water molecules. In the 2700–3700 cm^{-1} region, a strong broad peak is observed, which can be ascribed to the combined contributions of N–H stretching modes of NH_4^+ ions and O–H stretching vibrations of water molecules.

Guo *et al.* investigated the Raman spectra of aqueous ammonium nitrate droplets and demonstrated that the spectral features in the 2500–4000 cm^{-1} region can be reproduced by fitting with a superposition of six peaks centered at 2890, 3090, 3140, 3220, 3402, and 3507 cm^{-1}.[25] Following this work, peak-deconvolution fitting of the Raman spectra in Fig. 3 was

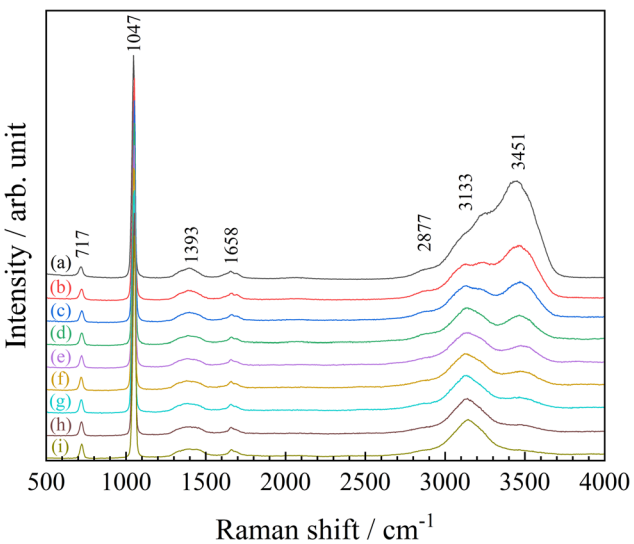

Fig. 3 Raman spectra of the optically levitated NH_4NO_3 aqueous droplet shown in Fig. 2 at different relative humidities. Spectra correspond to panels (a)–(i) in Fig. 2.

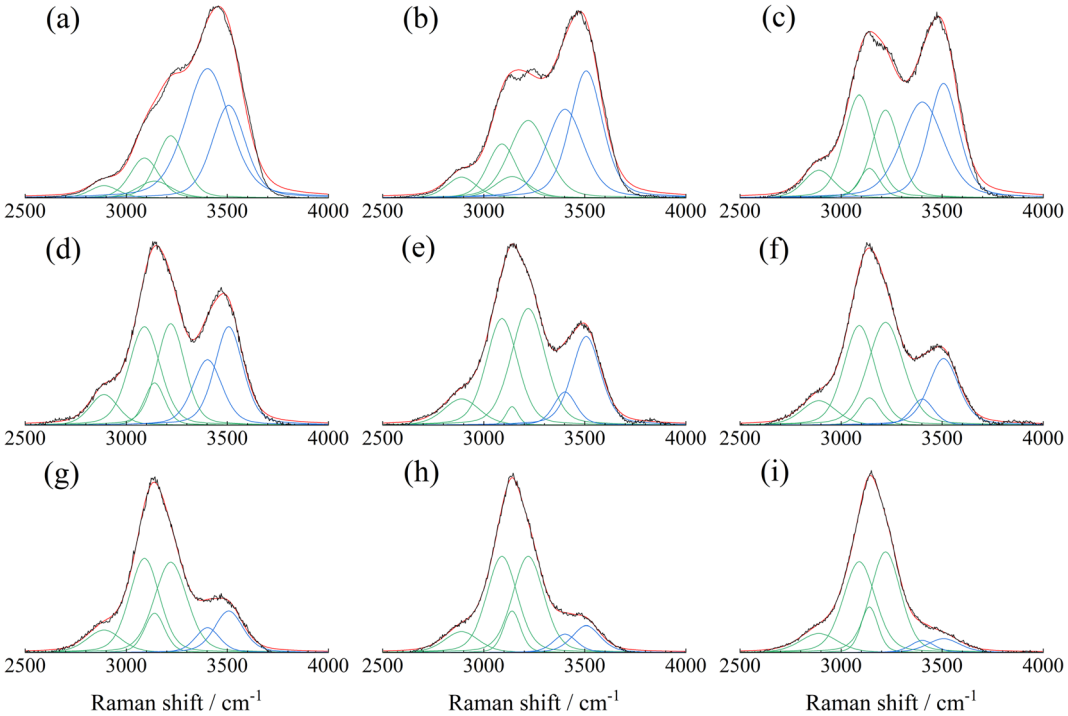

Fig. 4 Peak-deconvolution fitting of the Raman spectra (2500–4000 cm^{-1}) shown in Fig. 3, with x_c (center wavenumbers) at 2890, 3090, 3140, 3220, 3402, and 3507 cm^{-1}.

performed, as presented in Fig. 4. Each peak was represented by a pseudo-Voigt function given by the following equation:

$$y = y_0 + A\left[\mu\frac{2}{\pi}\frac{w}{4(x-x_c)^2+w^2} + (1-\mu)\frac{\sqrt{4\ln 2}}{\sqrt{\pi}w}\exp\left(-\frac{4\ln 2}{w^2}(x-x_c)^2\right)\right] \quad (1)$$

Here, y_0 is the offset, A is the area, x_c is the center wavenumber, w is the full width at half maximum, and μ is the profile-shape factor. The four peaks observed on the lower-wavenumber side are primarily associated with NH_4^+ ions. The peaks at 2890, 3090, 3140, and 3220 cm^{-1} correspond to the second overtone of the NH_4^+ umbrella bending mode, the combination band of the NH_4^+ umbrella bending and rocking vibrations, the symmetric stretching vibration, and the antisymmetric stretching vibration of NH_4^+, respectively. Here, we note that the band at ~3220 cm^{-1} does not arise exclusively from NH_4^+ vibrations, but may also include a contribution from strongly hydrogen-bonded water molecules.[26] In concentrated and supersaturated NH_4NO_3 solutions, however, the relative population of strongly hydrogen-bonded water decreases substantially, such that the 3220 cm^{-1} band is dominated by NH_4^+-related N–H vibrations, although a minor water contribution cannot be completely excluded. In contrast, the two peaks on the high-wavenumber side at 3402 and 3507 cm^{-1} mainly arise from the O–H stretching vibrations of water and are attributed to weakly hydrogen-bonded and weakest (or nearly non-hydrogen-bonded) O–H stretching modes of water, respectively.[26] Based on these assignments, the water-related O–H stretching contribution was quantified using the sum of the integrated areas of the 3402 cm^{-1} and 3507 cm^{-1} bands.

To estimate the ammonium nitrate concentration, the Raman peak at 1047 cm^{-1} attributed to the NO_3^- ion was fitted using eqn (1), and the corresponding peak area (A_{1047}) was obtained from the spectrum shown by the black solid line in Fig. 3. The peak-area ratio (A_R) was then calculated as the ratio of A_{1047} to the sum of the water-related peak areas at 3402 cm^{-1} (A_{3402}) and 3507 cm^{-1} (A_{3507}), where A_{3402} and A_{3507} were obtained from the peak-deconvolution analysis shown in Fig. 4(a).

$$A_R = \frac{A_{1047}}{A_{3402} + A_{3507}} \quad (2)$$

Using eqn (2), the A_R value of the droplet shown in Fig. 2(a) was calculated to be 0.171. Because A_R depends on the molar ratio of NO_3^- to H_2O, it is proportional to the molality (m) of the NH_4NO_3 aqueous solution. To construct a calibration curve, Raman spectra of bulk NH_4NO_3 aqueous solutions with known concentrations were measured (Fig. S1, SI). Peak-deconvolution fitting of the Raman spectra in the 2500–4000 cm^{-1} region was performed (Fig. S2), and the resulting A_R values were plotted as a function of m. As shown in Fig. S3, a good linear relationship was observed between A_R and m, with least-squares regression giving a slope of 0.023 ± 0.001 kg mol^{-1}, an intercept of 0.01 ± 0.01, and R^2 = 0.999. Using Fig. S3 as the calibration curve, the NH_4NO_3 concentration of the droplet shown in Fig. 2(a) was estimated to be 7.0 ± 0.8 mol kg^{-1}. The uncertainty (±0.8 mol kg^{-1}) represents the 95% confidence interval obtained by propagating the standard errors of the

Table 1 Physical and compositional properties of single optically levitated NH_4NO_3 aqueous droplets shown in Fig. 2(a)–(i)

Droplet	RH/%	Diameter/μm	m/mol kg^{-1}	x_I[a]	n[b]/mol
a	85.0	18.3	7.0 ± 0.8	0.20 ± 0.02	1.66×10^{-11}
b	72.2	15.6	14.7 ± 0.9	0.35 ± 0.02	1.66×10^{-11}
c	64.7	14.6	21 ± 1	0.43 ± 0.02	1.66×10^{-11}
d	52.3	13.6	37 ± 1	0.57 ± 0.02	1.66×10^{-11}
e	42.6	13.0	56 ± 2	0.67 ± 0.02	1.65×10^{-11}
f	36.0	12.8	69 ± 3	0.71 ± 0.03	1.65×10^{-11}
g	27.0	12.5	94 ± 4	0.77 ± 0.03	1.63×10^{-11}
h	16.8	12.2	138 ± 6	0.83 ± 0.03	1.61×10^{-11}
i	7.9	12.0	215 ± 9	0.89 ± 0.04	1.60×10^{-11}

[a] x_I is total ion mole fraction. [b] n is the amount of substance of NH_4NO_3 contained in the droplet.All measurements were performed at 25.0 ± 0.5 °C and ambient pressure (≈1 atm).

calibration-curve regression to the estimated m of the droplet. The calculated results are summarized in Table 1.

Thereafter, the relative humidity (RH) in the chamber was gradually lowered by adjusting the flow ratio of humidified and dry nitrogen. Over a period of approximately five hours, the RH decreased from 85.0% to 7.9%. Fig. 2(b)–(i) present a series of snapshots of the droplet taken during the dehydration process. As the surrounding gas phase was dehumidified, water evaporated from the optically trapped droplet in air, causing its diameter to gradually decrease. Fig. 3 shows the Raman spectra of the optically levitated NH_4NO_3 aqueous droplet shown in Fig. 2 at different relative humidities. As water evaporated from the droplets, a pronounced decrease in the intensity of the peak around 3451 cm^{-1} was observed. As described above, peak-deconvolution fitting of the Raman spectra in the 2500–4000 cm^{-1} region was performed for each spectrum (Fig. 4), and the resulting A_R values were used to calculate the molality of NH_4NO_3 for each droplet. The results are summarized in Table 1. As the relative humidity decreased from 85.0% to 7.9%, the NH_4NO_3 concentration in the droplet increased from 7.0 ± 0.8 to 215 ± 9 mol kg^{-1}.

Here, we note that the calibration curve was constructed from bulk aqueous solution data and is extrapolated to estimate molalities in the highly supersaturated regime. Nevertheless, as discussed in the following section, comparison with previously reported electrodynamic balance (EDB) measurements indicates that the resulting molalities are broadly consistent with EDB data at moderate supersaturations, supporting the use of the extrapolated calibration as an approximately reasonable estimate.

Since the saturated concentration of NH_4NO_3 at 25 °C is 26 mol kg^{-1},[4] the droplets shown in Fig. 2(d)–(i) correspond to supersaturated solutions. Notably, the droplet at RH = 7.9% shown in Fig. 2(i) still appears as a homogeneous spherical particle, indicating that no crystallization occurred even at a concentration as high as 215 ± 9 mol kg^{-1}. Furthermore, in the Raman spectra shown in Fig. 3, the NO symmetric stretching band exhibits a slight shift from 1047 to 1052 cm^{-1} as the NH_4NO_3 concentration increases from 7.0 mol kg^{-1} (a) to 215 mol kg^{-1} (i), corresponding to a shift toward higher wavenumbers. Although previous Raman measurements of supersaturated ammonium nitrate droplets deposited on solid substrates reported little or no shift until deep supersaturation was reached, the small upshift observed here at very high molalities is broadly consistent with the reported concentration-dependent trend.[9,25]

In contrast, the Raman spectrum of crystalline NH_4NO_3 measured for reference (Fig. S4) displays the NO symmetric stretching vibration at 1042 cm^{-1}, together with a characteristic antisymmetric stretching mode at 1286 cm^{-1}. Importantly, even at the highest concentration of 215 mol kg^{-1}, no Raman band is observed at 1286 cm^{-1}, as shown in Fig. 3. In addition, the Raman bands at 3402 and 3507 cm^{-1}, which correspond to the O–H stretching vibrations of water, are barely detectable even at the highest concentration of 215 mol kg^{-1} (Fig. 4(i)), but are completely absent in the crystalline sample (Fig. S4). Taken together, these observations unambiguously demonstrate that the droplets remain in a supersaturated aqueous state without undergoing efflorescence, even at a relative humidity as low as 7.9%.

3.2 Dependence of water activity on the total ionic mole fraction

According to Raoult's law, the activity of water decreases with increasing solute mole fraction. Since ammonium nitrate dissociates into NH_4^+ and NO_3^- ions in aqueous solution, the total ionic mole fraction, x_I, is defined by the following equation:

$$x_I = \frac{n(NH_4^+) + n(NO_3^-)}{n(NH_4^+) + n(NO_3^-) + n(H_2O)} \quad (3)$$

Here, $n(NH_4^+)$, $n(NO_3^-)$, and $n(H_2O)$ denote the amounts of substance of ammonium ions, nitrate ions, and water, respectively. The definition of x_I in eqn (3) implicitly assumes complete dissociation of NH_4NO_3 into NH_4^+ and NO_3^-. Possible formation of ion-paired or other associated species at high concentrations is therefore not explicitly considered. In addition, the autoionization of water, as well as the generation of OH^- ions through acid–base equilibria, are neglected in this definition, such that contributions from minor ionic species other than NH_4^+ and NO_3^- are not included. This simplified definition of x_I is adopted here to facilitate comparison with previous thermodynamic data. The values of x_I calculated from the molality m (mol kg^{-1}) of each droplet shown in Fig. 2(a)–(i) are summarized in Table 1.

At thermodynamic equilibrium, the activity of water in the droplet is related to the ambient RH through Raoult's law together with the curvature (Kelvin) correction:

$$\frac{RH}{100\%} = a_w \exp\left(\frac{2\sigma V_w}{RTr}\right) \quad (4)$$

where σ is the surface tension of the solution, V_w is the partial molar volume of water (1.81×10^{-5} m^3 mol^{-1}), R is the gas constant (8.314 J mol^{-1} K^{-1}), T is temperature, and r is the droplet radius. For the droplet shown in Fig. 2(a), the surface tension of a 7.0 mol kg^{-1} NH_4NO_3 aqueous solution at 298.15 K is estimated to be approximately 78.0 mN m^{-1}, interpolated from literature data.[27] At r = 9.2 μm, the exponential term is

effectively unity (≈1.00), indicating that the curvature effect is negligible for the micrometer-scale droplets investigated in this study. Therefore, we use $a_w \approx$ RH/100% to convert RH to water activity. Using this relation, a_w is plotted as a function of the total ionic mole fraction x_I for the data sets in Fig. 2(a)–(i), as shown by the red circles in Fig. 5. Results from analogous experiments performed on different droplets are indicated by stars and diamonds, respectively, and the corresponding data are provided in Tables S2 and S3 of the SI. For comparison, Fig. 5 also includes bulk-solution literature data,[4] Kusik–Meissner (KM) model calculations based on the EDB measurements of Chan *et al.*,[6] and EDB literature data reported by Lightstone *et al.*,[14] shown as open triangles, open squares, and open diamonds, respectively. The arrow in Fig. 5 denotes the saturation concentration at 25 °C.

The EDB experimental results reported by Chan *et al.* (open squares in Fig. 5) were analyzed under the assumption that the loss of NH_4NO_3 due to volatilization is negligible, such that the amount of NH_4NO_3 contained in the droplet remains constant throughout the experiment.[6] In contrast, the EDB results reported by Lightstone *et al.* (open diamonds in Fig. 5) were analyzed with consideration of NH_4NO_3 volatilization. They reported that the loss of NH_4NO_3 from aqueous droplets due to volatilization is negligible at relative humidities above 40%, whereas the effect becomes significant under lower-humidity conditions.[14]

To examine whether this interpretation is also applicable to our experiments, the amount of NH_4NO_3 contained in the droplet, n, was evaluated as follows. First, the molality derived from Raman spectroscopic analysis was converted to molar concentration using solution density data. The droplet volume was independently determined from two-dimensional image analysis assuming a spherical geometry, and the amount of NH_4NO_3 was obtained by multiplying the molar concentration by this volume. The density of the aqueous NH_4NO_3 solution used for this conversion was calculated using literature parameterizations,[28] and detailed numerical values are summarized in the SI (Table S1). The resulting n values are summarized in Table 1.

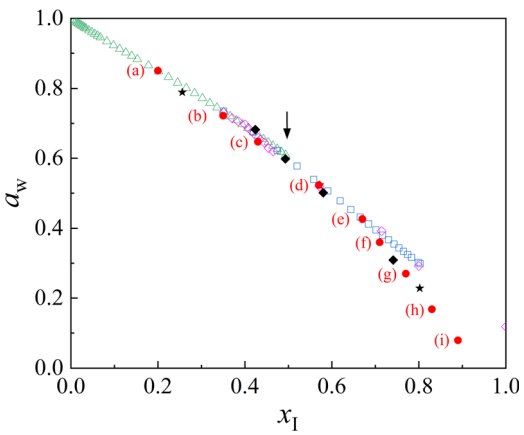

Fig. 5 Water activity (a_w) as a function of total ionic mole fraction (x_I) for ammonium nitrate solutions at 25 °C. Red circles denote data obtained from the droplet shown in Fig. 2; stars and diamonds indicate measurements from additional droplets. Open triangles represent bulk-solution literature data (Wishaw and Stokes, 1953).[4] Open squares show Kusik–Meissner model calculations based on electrodynamic-balance (EDB) measurements by Chan *et al.* (1992),[6] and open diamonds indicate EDB data reported by Lightstone *et al.* (2000).[14] The arrow marks the saturation concentration at 25 °C.

At relative humidities between 85.0% and 52.3%, n remains essentially constant at 1.66×10^{-11} mol. With further decreases in relative humidity, however, n gradually decreases, reaching 1.60×10^{-11} mol at RH = 7.9%. This trend is broadly consistent with the interpretation proposed by Lightstone *et al.* Consequently, as shown in Fig. 5, in the region where the relative humidity exceeds 40% (*i.e.*, $a_w \geq 0.4$), our experimental results are in good agreement with the reported literature values.

It is noteworthy that a systematic deviation from the EDB data becomes apparent as x_I increases beyond 0.67 (corresponding to $a_w < 0.4$). This discrepancy is most likely attributable to differences in the treatment of NH_4NO_3 volatilization and, consequently, in the estimation of the solute amount remaining in the droplet. In the study by Lightstone *et al.*, volatilization losses were evaluated by returning the droplet to a fixed reference relative humidity after each low-RH measurement and using the resulting mass change as a correction. While this approach provides a practical means of accounting for volatilization in EDB experiments, its accuracy may depend on the humidity-ramp protocol and the assumptions underlying the reference-state correction.

In contrast, in the present study, the NH_4NO_3 concentration at each relative humidity was determined directly from *in situ* Raman spectroscopic measurements combined with spectral deconvolution analysis. Although the present measurements do not demonstrate that a_w strictly reaches zero at $x_I = 1.0$, the data exhibit a systematic deviation toward lower a_w values compared with those reported by Lightstone *et al.* as x_I increases. Considering that Lightstone *et al.* reported a finite value of $a_w = 0.118$ at $x_I = 1.0$, as shown in Fig. 5, the observed deviation toward smaller a_w values at high x_I may be interpreted as a physically reasonable tendency in the highly supersaturated regime.

To further assess whether the amount of NH_4NO_3 in the droplet estimated from Raman spectroscopic measurements (the n values in Table 1) is reasonable, an order-of-magnitude consistency check was performed using representative volatilization fluxes reported in the literature.[16] Lu *et al.* reported NH_4NO_3 volatilization fluxes from optically trapped droplets at 298 K on the order of 10^{-8}–10^{-7} mol s^{-1} m^{-2}.[16] Using a representative value of 1.0×10^{-7} mol s^{-1} m^{-2} within this range, together with the droplet radius of 6.0 μm for the droplet in Fig. 2(i) (surface area $\approx 4.5 \times 10^{-10}$ m^2) and the elapsed time of 275 min (1.65×10^4 s) required for the dehumidification process from Fig. 2(a)–(i), the amount of NH_4NO_3 potentially lost by volatilization is estimated to be $\sim 7.4 \times 10^{-13}$ mol. The experimentally determined decrease in n between Fig. 2(a) and (i) is 6×10^{-13} mol (Table 1), which is of the same order as the above estimate. While this comparison is not intended as a quantitative validation, it supports the view that the

Raman-based n values obtained in the present study are physically plausible.

3.3 Osmotic coefficient and mean molal ionic activity coefficient of ammonium nitrate in supersaturated solutions

For electrolytes such as ammonium nitrate, the thermodynamic behavior of the solution is conveniently described in terms of the mean molal ionic activity coefficient, $\gamma_{\pm}$. On the molality scale, the mean ionic activity of the solute, $a_{\pm}$, is defined as

$$a_{\pm} = \frac{m}{m^{\circ}}\gamma_{\pm}, \quad \left(m^{\circ} = 1 \text{ mol kg}^{-1}\right) \tag{5}$$

where m denotes the molality of ammonium nitrate (NH_4NO_3), equivalently written as $m_{\pm}$, defined as the number of moles of NH_4NO_3 per kilogram of water.

The Gibbs–Duhem equation expressed on the molality scale is

$$\nu m\, d\ln a_{\pm} + \left(\frac{1}{M_W}\right) d\ln a_w = 0 \tag{6}$$

where ν is the stoichiometric number of ions produced upon dissociation (ν = 2 for $NH_4NO_3 \rightarrow NH_4^+ + NO_3^-$), a_w is the activity of water, and M_w is the molar mass of water expressed in units of kg mol^{-1}.

The activity of water is related to the molal osmotic coefficient, ϕ, through

$$\ln a_w = -M_w \nu m \phi. \tag{7}$$

Combining eqn (5)–(7) yields the following differential relation for the mean ionic activity coefficient:

$$d\ln\gamma_{\pm} = \frac{\phi - 1}{m}\mathrm{d}m + \mathrm{d}\phi. \tag{8}$$

Integration from infinite dilution to a finite molality m gives

$$\int_0^m d\ln\gamma_{\pm} = \int_0^m \frac{\phi - 1}{m'}dm' + \int_0^m d\phi \tag{9}$$

where m' is the integration variable. Using the boundary conditions $\gamma_{\pm} \rightarrow 1$ and $\phi \rightarrow 1$ as $m \rightarrow 0$, one obtains

$$\ln\gamma_{\pm}(m) = \int_0^m \frac{\phi(m') - 1}{m'}dm' + [\phi(m) - 1]. \tag{10}$$

Accordingly, the mean ionic activity coefficient $\gamma_{\pm}(m)$ of ammonium nitrate can be determined from experimentally measured water activity data. The osmotic coefficient $\phi(m)$ is first obtained from eqn (7), and the corresponding $\gamma_{\pm}(m)$ is then calculated using eqn (10).

Using eqn (4), the relative humidity during the dehumidification process of the water droplets was converted to the water activity, a_w. The osmotic coefficient, ϕ, was then calculated from a_w using eqn (7). During the dehumidification process, the droplet was continuously observed under a microscope in bright-field mode, and the laser power was manually adjusted to maintain stable optical trapping by balancing the radiation pressure of the laser against gravity. By contrast, Raman spectra had to be recorded under dark-field conditions with the microscope illumination turned off. As a result, Raman spectra of the droplet were acquired at intervals of approximately 30 min, and consequently were obtained only at the nine discrete points listed in Table 1. When determining the mean molal ionic activity coefficient, $\gamma_{\pm}(m)$, by integrating the osmotic coefficient ϕ using eqn (10), the Raman data alone are therefore too sparsely spaced to allow accurate numerical integration.

To address this limitation, the temporal evolution of the droplet size between successive Raman measurements was continuously recorded as video images. These images were analyzed using ImageJ, and the molality values derived from Raman spectroscopy were interpolated based on the continuously measured droplet size. Specifically, the amount of NH_4NO_3 estimated from Raman spectroscopy, denoted as n in Table 1, was divided by the droplet volume—determined from the droplet radius obtained by image analysis—to yield the molar concentration. This value was then converted to molality, m, using literature density data.[28] Detailed numerical values are summarized in the SI (Table S1).

Fig. 6 shows ϕ plotted as a function of the molality, m, of ammonium nitrate. Solid circles in Fig. 6 denote data obtained from the droplet shown in Fig. 2, whereas stars and diamonds represent measurements performed on other droplets; the corresponding data are provided in Tables S2 and S3 of the SI, respectively. For the range $m < 26$ mol kg^{-1}, literature values of the osmotic coefficient, ϕ, for bulk aqueous solutions are shown as open triangles in Fig. 6.[4]

Pitzer-type ion-interaction models provide a widely used framework for describing electrolyte solutions.[29] In a previous study employing the EDB technique, Chan *et al.* analyzed experimental values of the osmotic coefficient, ϕ, of ammonium nitrate in the supersaturated concentration regime using the Pitzer model.[6] To reproduce the observed behavior of ϕ in

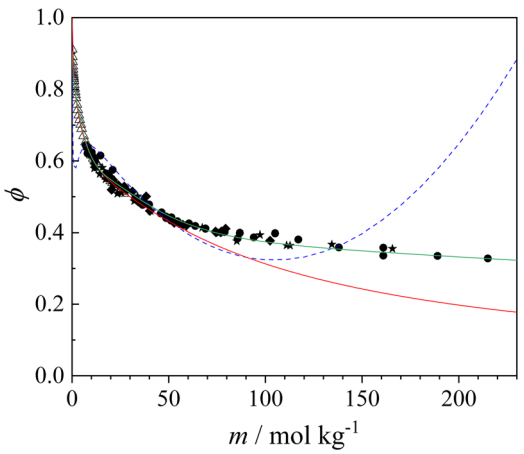

Fig. 6 Osmotic coefficient (ϕ) of aqueous NH_4NO_3 as a function of molality (m) at 25 °C. Solid circles correspond to the droplet shown in Fig. 2, while stars and diamonds represent measurements from other droplets. Open triangles indicate bulk-solution literature data. The blue dashed line shows Pitzer-model calculations using the modified parameters proposed by Chan *et al.* (1992).[6] the red and green solid lines show BIMSA model predictions based on the parameter set of Simonin *et al.* and the modified parameters obtained in this study, respectively.

this regime, Chan *et al.* proposed a modified set of fitting parameters for the Pitzer model equations. The corresponding results are shown as the blue dashed line in Fig. 6. These parameters provide a reasonable approximation to the experimental data in the range from 10 to approximately 50 mol kg^{-1}; however, at higher concentrations, the calculated values of ϕ increase sharply, leading to a significant deviation from the experimental data. We also attempted to optimize the Pitzer-model parameters to reproduce our experimental results, but satisfactory agreement in the high-concentration region could not be achieved. Consequently, in the present study, we adopted an alternative numerical modeling approach to describe the molality dependence of ϕ for NH_4NO_3 shown in Fig. 6 instead of the Pitzer model.

The binding mean spherical approximation (BIMSA) is an MSA-based associative framework in which ion pairing is incorporated self-consistently through a mass-action law.[30,31] Simonin *et al.* demonstrated that the osmotic coefficients of aqueous NH_4NO_3 solutions can be successfully described by the BIMSA model up to near-saturation concentrations (25 mol kg^{-1}).[23] In this approach, ion pairing is introduced through an association constant K, and the ion–pair number density ρ_p is obtained from the mass-action law:

$$K_0 = \frac{\rho_p}{(\rho_+\alpha_+)(\rho_-\alpha_-)} = K g_c^{HS} \exp\left[-2\lambda \frac{z'_+ z'_- - z_+ z_- (\varepsilon/\varepsilon_w)}{\sigma_p}\right] \quad (11)$$

where ρ_+ and ρ_- are the total number densities of cations and anions, α_+ and α_- are the fractions of unbound ions, g_c^{HS} is the contact hard-sphere probability, and $\sigma_p = \sigma_+ + \sigma_-$ is the contact distance between ions, with σ_+ and σ_- denoting the diameters of cations and anions, respectively. The quantities z_+ and z_- are the ionic valences, while z'_+ and z'_- represent the MSA effective charges that incorporate screening and finite-size effects. The electrostatic prefactor is defined as $\lambda \equiv \beta e^2/(4\pi\varepsilon_0\varepsilon)$, where $\beta = 1/(k_B T)$, ε_0 is the permittivity of a vacuum, ε and ε_w are the relative permittivities of the solution and pure water, respectively.

Solvation effects are represented by allowing the effective cation diameter and the relative permittivity to vary linearly with the electrolyte molar concentration C_s, while treating the anion diameter as constant:

$$\sigma_+ = \sigma^{(0)} + \sigma^{(1)} C_s \quad (12)$$

$$\varepsilon^{-1} = \varepsilon_w{}^{-1}(1 + \alpha C_s) \quad (13)$$

where, $\sigma^{(0)}$, $\sigma^{(1)}$ and α are adjustable parameters. With these parameters optimized, the BIMSA model provides an accurate description of thermodynamic properties in the near-saturated regime. The parameter set for NH_4NO_3 reported by Simonin *et al.* is summarized in Table 2.[23] Using these parameters, we implemented the BIMSA equations in a Python program and calculated the concentration dependence of the osmotic coefficient; the resulting curve is shown as the red solid line in Fig. 6.

As shown in Fig. 6, the osmotic coefficient ϕ calculated using the parameters of Simonin *et al.* agrees well with experimental data up to about 50 mol kg^{-1}, while deviations become apparent at higher concentrations, where the model underestimates ϕ. This behavior suggests that linear concentration dependencies in the effective solvation parameters may become inadequate at very high concentrations. Accordingly, and with accurate reproduction of the measured osmotic coefficients over the entire range as the primary objective, we adopt a BIMSA-based semi-empirical representation in which the effective parameters are allowed to vary smoothly with concentration. Specifically, we generalize the concentration dependence of σ_+ and ε by including quadratic terms:

$$\sigma_+ = \sigma^{(0)} + \sigma^{(1)} C_s + \sigma^{(2)} C_s{}^2 \quad (14)$$

$$\varepsilon^{-1} = \varepsilon_w{}^{-1}(1 + \alpha C_s + \alpha_2 C_s{}^2) \quad (15)$$

where, $\sigma^{(2)}$ and α_2 are fitting constants.

The parameters were estimated by nonlinear least-squares regression against the experimental osmotic-coefficient data in Fig. 6 and are summarized in Table 2. Using these optimized parameters, the osmotic coefficient ϕ computed within this BIMSA-based, concentration-dependent parameterization is shown as the green solid line in Fig. 6. This formulation provides a consistent representation of the data across the full experimental range, including the newly accessed ultra-high-molality region.

Thus, having obtained a mathematical representation of the experimental osmotic-coefficient data, we next calculated the mean molal ionic activity coefficient using eqn (10). In principle, evaluation of $\gamma_\pm(m)$ with this expression requires integration from infinite dilution. However, in the present experiments for the droplet shown in Fig. 2, the lowest molality of NH_4NO_3 was 7.0 mol kg^{-1} (see Table 1). Accordingly, the value of $\gamma_\pm$ at 7.0 mol kg^{-1} was calculated using the Extended Aerosol Inorganics Model (E-AIM) and employed as the initial condition for the integration.[32] The resulting activity coefficients are shown as solid circles in Fig. 7, and the full dataset is summarized in the SI (Table S1). The same measurements and analysis were performed for two additional droplets; the corresponding results are shown as stars and diamonds in Fig. 7, with the data provided in Tables S2 and S3 of the SI, respectively. In addition, predictions of the BIMSA model using the modified parameters obtained in this study and listed in Table 2 are shown as the green solid line.

To date, the EDB data reported by Chan *et al.* represent the highest-concentration direct measurements available at 25 °C for the osmotic coefficient and the mean molal ionic activity coefficient of aqueous NH_4NO_3.[6] Consequently, prior

Table 2 BIMSA model parameters and their maximum applicable molality

	Simonin *et al.* (1998)[23]	This Study
$\sigma^{(0)}$/m	3.33×10^{-10}	3.33×10^{-10}
$\sigma^{(1)}$/m mol^{-1} L	-2.00×10^{-12}	-4.49×10^{-11}
$\sigma^{(2)}$/m mol^{-2} L^2		2.40×10^{-12}
α/mol^{-1} L	6.13×10^{-2}	-3.20×10^{-2}
α_2/mol^{-2} L^2		1.42×10^{-4}
K/mol^{-1} L	0.338	0.865
Maximum applicable molality, m/mol kg^{-1}	25	215

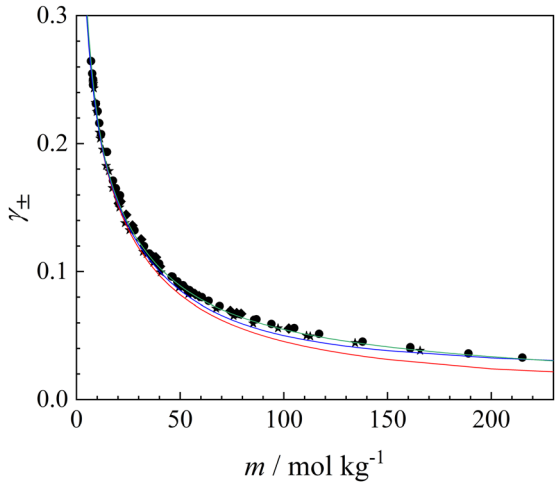

Fig. 7 Mean molal ionic activity coefficient ($\gamma_{\pm}$) of NH_4NO_3 as a function of molality (m) at 25 °C. Symbols are defined as in Fig. 6. The green solid line shows predictions of the BIMSA-based model using the optimized parameters obtained in this study. Predictions from the E-AIM and the AIOMFAC model are shown by the red and blue solid lines, respectively.

experimental values at 25 °C have been limited to molalities of up to approximately 111 mol kg^{-1}. As shown in Fig. 6 and 7, to the best of our knowledge, the present study provides the first successful experimental determination of the osmotic coefficient and mean molal ionic activity coefficient of aqueous NH_4NO_3 up to m = 215 mol kg^{-1}.

Recent studies have highlighted notable discrepancies between thermodynamic predictions obtained using the E-AIM and the Aerosol Inorganic–Organic Mixtures Functional groups Activity Coefficients (AIOMFAC) model,[33,34] both of which are widely used in aerosol thermodynamics, particularly under highly concentrated or supersaturated conditions.[3] Motivated by these reported differences, we therefore compare our experimentally determined mean molal ionic activity coefficients with the corresponding model predictions. The results from the E-AIM (https://www.aim.env.uea.ac.uk/aim/aim.php) and AIOMFAC (https://aiomfac.lab.mcgill.ca) models are included as the red and blue solid lines in Fig. 7, respectively.

In the supersaturated concentration region newly explored in this work, AIOMFAC appears to reproduce the observed mean molal ionic activity coefficients of NH_4NO_3 more closely than E-AIM when the latter is extrapolated beyond its original calibration range. Both E-AIM and AIOMFAC are semi-empirical models based on Pitzer-type ion-interaction formulations and therefore differ in theoretical framework from the BIMSA approach used here. Because these models are parameterized by fitting to experimental data, the present measurements provide valuable benchmarks and may facilitate future refinement and extension of model applicability toward higher concentrations.

4. Conclusions

In this study, micrometer-sized aqueous droplets containing NH_4NO_3 were levitated in air using a laser trapping technique, enabling continuous concentration increase up to m = 215 mol kg^{-1} by controlled reduction of relative humidity. The measured water activities agree well with literature data over the range x_I = 0.20–0.67, while systematic deviations from EDB-derived values are observed at higher ionic fractions. This difference likely reflects the distinct experimental constraints: whereas EDB measurements estimate solution composition from the particle mass decrease measured after dehydration–rehydration cycling, the present approach directly constrains droplet composition *in situ* by Raman spectroscopy, providing additional insight under extreme concentration conditions.

New osmotic-coefficient data were obtained over an unprecedented molality range, revealing pronounced non-ideal behavior at high molalities. To describe these data, a BIMSA-based framework was adopted, yielding a compact and internally consistent representation of the osmotic coefficient across the full experimental range. The corresponding mean molal ionic activity coefficients at high molalities provide valuable benchmarks for evaluating thermodynamic models, particularly given the discrepancies among existing predictions in the supersaturated regime.

Future work will extend this experimental approach to multicomponent inorganic and organic–inorganic systems relevant to atmospheric aerosols and microdroplet environments. In addition, an important direction for future research is to investigate the temperature dependence of the thermodynamic properties of aqueous ammonium nitrate. In particular, experimental data covering a broader temperature range, especially toward lower temperatures relevant to atmospheric conditions, remain scarce. We have previously developed an experimental system capable of cooling optically levitated droplets down to 198 K using liquid nitrogen.[35] This capability will enable future studies of temperature effects on thermodynamic properties, such as water activity, the osmotic coefficient, and the mean molal ionic activity coefficient, under supersaturated and supercooled conditions.

Author contributions

Kento Kuniyoshi: investigation, writing – original draft. Shoji Ishizaka: writing – review & editing, supervision, funding acquisition.

Conflicts of interest

The authors declare that they have no known competing financial interests or personal relationships that could have appeared to influence the work reported in this paper.

Data availability

The data that support the findings of this study are available within the article and its supplementary information (SI). Supplementary information is available. See DOI: https://doi.org/10.1039/d6cp01016d.

Acknowledgements

This research was supported by the JSPS KAKENHI Grant Numbers JP21H01964.

References

1 M. Y. Wang, W. M. Kong, R. Marten, X. C. He, D. X. Chen, J. Pfeifer, A. Heitto, J. Kontkanen, L. Dada, A. Kurten, T. Yli-Juuti, H. E. Manninen, S. Amanatidis, A. Amorim, R. Baalbaki, A. Baccarini, D. M. Bell, B. Bertozzi, S. Bräkling, S. Brilke, L. C. Murillo, R. Chiu, B. W. Chu, L. P. De Menezes, J. Duplissy, H. Finkenzeller, L. G. Carracedo, M. Granzin, R. Guida, A. Hansel, V. Hofbauer, J. Krechmer, K. Lehtipalo, H. Lamkaddam, M. Lampimäki, C. P. Lee, V. Makhmutov, G. Marie, S. Mathot, R. L. Mauldin, B. Mentler, T. Muller, A. Onnela, E. Partoll, T. Petäjä, M. Philippov, V. Pospisilova, A. Ranjithkumar, M. Rissanen, B. Rörup, W. Scholz, J. L. Shen, M. Simon, M. Sipilä, G. Steiner, D. Stolzenburg, Y. J. Tham, A. Tomé, A. C. Wagner, D. Y. S. Wang, Y. H. Wang, S. K. Weber, P. M. Winkler, P. J. Wlasits, Y. H. Wu, M. Xiao, Q. Ye, M. Zauner-Wieczorek, X. Q. Zhou, R. Volkamer, I. Riipinen, J. Dommen, J. Curtius, U. Baltensperger, M. Kulmala, D. R. Worsnop, J. Kirkby, J. H. Seinfeld, I. El-Haddad, R. C. Flagan and N. M. Donahue, *Nature*, 2020, **581**, 184–189.
2 R. X. Ward, H. D. Baliaka, B. C. Schulze, G. H. Kerr, J. D. Crounse, S. Hasheminassab, R. Bahreini, A. M. Dillner, A. Russell, N. L. Ng, P. O. Wennberg, R. C. Flagan and J. H. Seinfeld, *Sci. Adv.*, 2025, **11**, eadt8957.
3 R. L. Wan, G. J. Zheng, Y. Y. Li, X. L. Duan, J. K. Jiang and K. B. He, *Atmos. Chem. Phys.*, 2026, **26**, 1795–1807.
4 B. F. Wishaw and R. H. Stokes, *Trans. Faraday Soc.*, 1953, **49**, 27–31.
5 W. J. Hamer and Y. C. Wu, *J. Phys. Chem. Ref. Data*, 1972, **1**, 1047–1099.
6 C. K. Chan, R. C. Flagan and J. H. Seinfeld, *Atmos. Environ., Part A*, 1992, **26**, 1661–1673.
7 S. S. Ma, S. F. Pang, J. Li and Y. H. Zhang, *Chemosphere*, 2021, **277**, 130320.
8 I. N. Tang, *J. Geophys. Res.: Atmos.*, 1996, **101**, 19245–19250.
9 M. C. Yeung and C. K. Chan, *Aerosol. Sci. Technol.*, 2010, **44**, 269–280.
10 P. G. Dougle, J. P. Veefkind and H. M. ten Brink, *J. Aerosol Sci.*, 1998, **29**, 375–386.
11 D. J. Cziczo and J. P. D. Abbatt, *J. Phys. Chem. A*, 2000, **104**, 2038–2047.
12 C. B. Richardson and R. L. Hightower, *Atmos. Environ.*, 1987, **21**, 971–975.
13 Y. J. Li, P. F. Liu, C. Bergoend, A. P. Bateman and S. T. Martin, *Aerosol. Sci. Technol.*, 2017, **51**, 388–396.
14 J. M. Lightstone, T. B. Onasch, D. Imre and S. Oatis, *J. Phys. Chem. A*, 2000, **104**, 9337–9346.
15 S. Ishizaka, F. Q. Guo, X. M. Tian, S. Seng, Y. A. Tobon and S. Sobanska, *Bull. Chem. Soc. Jpn.*, 2020, **93**, 86–91.
16 X. J. Lü, X. Y. Gao, J. B. Ma and Y. H. Zhang, *Spectrosc. Spectral Anal.*, 2019, **39**, 1648–1652.
17 D. W. Hu, J. M. Chen, X. N. Ye, L. Li and X. Yang, *Atmos. Environ.*, 2011, **45**, 2349–2355.
18 S. Ishizaka, K. Yamauchi and N. Kitamura, *Anal. Sci.*, 2013, **29**, 1223–1226.
19 S. Ishizaka, K. Yamauchi and N. Kitamura, *Anal. Sci.*, 2014, **30**, 1075–1079.
20 S. Ishizaka, C. Yamamoto and H. Yamagishi, *J. Phys. Chem. A*, 2021, **125**, 7716–7722.
21 Y. Tanaka and S. Ishizaka, *Anal. Sci.*, 2024, **40**, 123–132.
22 N. Tyumyo, G. Bourdon, E. Villenave, S. Sobanska and S. Ishizaka, *Chemosphere*, 2025, **385**, 144581.
23 J. P. Simonin, O. Bernard and L. Blum, *J. Phys. Chem. B*, 1998, **102**, 4411–4417.
24 H. C. Tang and B. H. Torrie, *J. Phys. Chem. Solids*, 1977, **38**, 125–138.
25 X. Guo, S. H. Tan, Z. J. Shang, Y. C. Guo and Y. H. Zhang, *Acta Phys.-Chim. Sin.*, 2012, **28**, 766–772.
26 P. Kim, W. Xiong and R. E. Continetti, *J. Phys. Chem. B*, 2020, **124**, 9385–9395.
27 S. Mosallanejad, I. Oluwoye, M. Altarawneh, J. Gore and B. Z. Dlugogorski, *Phys. Chem. Chem. Phys.*, 2020, **22**, 27698–27712.
28 S. L. Clegg and A. S. Wexler, *J. Phys. Chem. A*, 2011, **115**, 3393–3460.
29 K. S. Pitzer and G. Mayorga, *J. Phys. Chem.*, 1973, **77**, 2300–2308.
30 J. P. Simonin, L. Blum and P. Turq, *J. Phys. Chem.*, 1996, **100**, 7704–7709.
31 J. P. Simonin, *J. Phys. Chem. B*, 1997, **101**, 4313–4320.
32 S. L. Clegg, P. Brimblecombe and A. S. Wexler, *J. Phys. Chem. A*, 1998, **102**, 2155–2171.
33 A. Zuend, C. Marcolli, B. P. Luo and T. Peter, *Atmos. Chem. Phys.*, 2008, **8**, 4559–4593.
34 A. Zuend, C. Marcolli, A. M. Booth, D. M. Lienhard, V. Soonsin, U. K. Krieger, D. O. Topping, G. McFiggans, T. Peter and J. H. Seinfeld, *Atmos. Chem. Phys.*, 2011, **11**, 9155–9206.
35 S. Ishizaka, T. Wada and N. Kitamura, *Chem. Phys. Lett.*, 2011, **506**, 117–121.